Electronic Supplementary Material (ESI) for Green Chemistry.

Supporting Information

Reductive deconstruction of organosolv lignin catalyzed by zeolite supported Ni nanoparticles

Stanislav Kasakov[a], Hui Shi[b], Donald M. Camaioni[b], Chen Zhao[a,c], Eszter Baráth[a]*, Andreas Jentys[a], Johannes A. Lercher[a,b]*

[a]Technische Universität München, Department Chemie, Lichtenbergstraβe 4, Garching, D-85748, Germany
[b]Institute for Integrated Catalysis, Pacific Northwest National Laboratory, 902 Battelle Boulevard, Richland, WA 99352, USA
[c]Current address: Department of Chemistry, East China Normal University, North Zhongshan Road 3663, 200062, Shanghai, China

*Corresponding author: Eszter Baráth, Eszter.Barath@tum.de; Johannes A. Lercher, Johannes.Lercher@ch.tum.de

Table S1. Acid concentrations of parent support materials.

Support	Si/Al ratio	Acidity (μmol·g^{-1})[a]	
		BAS	LAS
HZSM-5	45	360	46
HBEA	75	190	41
SiO_2	–	-	-

[a] Determined by Pyridine-IR.

Table S2. Physicochemical properties of bare supports and Ni catalysts.

Support/ Catalyst	BET surface area [m^2 g^{-1}]			Pore volume [cm^3 g^{-1}]		
	Micro	Meso	Total	Micro	Meso	Total
HZSM-5	369	55	424	0.17	0.12	0.29
Ni/HZSM-5	243	108	351	0.12	0.15	0.27
HBEA	289	180	469	0.19	0.34	0.53
Ni/HBEA	76	332	408	0.04	0.47	0.51
SiO_2	27	160	187	0.04	0.26	0.30
Ni/SiO_2	18	239	257	0.08	0.65	0.73

The physicochemical properties of parent supports as well as the Ni incorporated catalysts are summarized in **Table S2**. The zeolites showed higher specific surface areas, i.e., 469 m^2 g^{-1} for HBEA and 424 m^2 g^{-1} for HZSM-5, than silica with 187 m^2 g^{-1}. In comparison with HZSM-5, the Ni/HZSM-5 sample exhibited a smaller surface area of 351 m^2 g^{-1}; specifically, the mesoporous fraction increased by more than twice (55 m^2 g^{-1} for parent HZSM-5 and 108 m^2 g^{-1} for Ni/HZSM-5), whereas the micropore fraction decreased from 369 m^2 g^{-1} (parent HZSM-5) to 243 m^2 g^{-1} (Ni/HZSM-5). Similarly, for HBEA, the surface area reduced from 469 to 408 m^2 g^{-1} upon Ni incorporation, where mesopores increased by almost twofold (180 m^2 g^{-1} for HBEA and 332 m^2 g^{-1} for Ni/HBEA, respectively) and micropores reduced by four times (289 vs 76 m^2 g^{-1}). These changes of the textural properties of support materials upon loading ca. 21% Ni are caused, in part, by the deposition precipitation procedure due to the acidic nature of aqueous suspension (pH ~ 2) during synthesis. Although urea decomposition generates *in situ* hydroxyl ions, which neutralizes the aqueous stirred suspension, the final mixture is still slightly acidic at pH ~ 5. [1-3] The distribution of pore sizes changed as well after synthesis.

The change of the textural properties can be explained by the hydrolytic degradation of the siliceous lattice during the acidic aqueous synthesis and the blockage of micropores by the deposited Ni particles. However, the change of the structural integrity of the support materials is beyond the scope of this work.

Table S3. Varying reaction conditions for optimizing Organosolv Lignin conversion [a].

Entry	Organosolv Lignin (g)	Ni/HBEA (g)	Temperature (K)	Initial H_2 pressure (bar)	Liquid phase HC yield (wt. %)
1	1	0.5	523	50	33
2	1	0.5	523	20	35
3	0.5	0.25	523	20	35
4	0.5	0.25	523	10	32
5	0.5	0.25	543	20	36
6	0.5	0.25	493	20	27
7	0.5	0.25	473	20	14
8	0.5	0.25	453	20	7
9	4	2	523	20	35
10	1	0.2	523	20	14

[a] General reaction conditions: 100 ml *n*-$C_{16}H_{34}$, 700 RPM, reaction duration 4 hours.

In order to elucidate the impact of reaction conditions, we have carried out a series of reactions varying the pressure from 50 to 10 bar (entry 1 – 4, **Table S3**), the temperature from 453 to 543 K (entry 5 – 8) and catalyst to lignin ratio from 0.5 to 0.2 (entry 9 and 10) with the best performing catalyst, i.e., 21 wt. % Ni/HBEA prepared by deposition precipitation. The experiment in the first entry was performed at the standard set of reaction conditions, with a H_2 initial pressure of 50 bar as performed in our previous hydrodeoxygenation studies [4-7]. Decreasing the hydrogen pressure to 20 bar (40 and 30 bar H_2, not shown here) slightly increased the liquid phase hydrocarbon yield by 2 wt. % (entry 3). A further decrease of the hydrogen pressure to 10 bar (entry 4) led to a comparable yield as the first entry with 32 wt. %. This finding is in accordance with the studies on aryl ether cleavage, where the variation of the initial hydrogen pressure caused a maximum in the rates of Ni catalyzed hydrogenolysis.[8]

Increasing the temperature from 523 to 543 K led to a marginal improvement of hydrocarbon yield by merely 1 wt. % (entry 5), whereas lowering the temperatures from 523 to 453 K resulted in a substantial loss of desired products, 27 wt. % at 493 K (entry 6), 14 wt.% at 473 K and 7 wt. % at 453 K, respectively (entries 7 and 8).

The effects of catalyst-to-lignin ratios, as well as the absolute weight of lignin and catalyst in the batch reactor, can be evaluated by looking at the entries 3 – 10. Changing the weights of catalyst and lignin, while keeping the catalyst-to-lignin ratio identical, did not affect product yields (entry 2, 3 and 9). The catalyst-to-lignin weight ratio of 0.5 resulted in the best yields (compare entries 2, 3, 5 and 9). Reducing this ratio to 0.2 caused the liquid hydrocarbon yield to decrease by a factor of 2.5 (entry 10), proportional to the decrease in the catalyst-to-lignin weight ratio.

Table S4. The stretching vibrational frequencies of aliphatic C-H and aliphatic C-H with carbon attached to oxygen (all numbers in cm^{-1}) [9].

Group	Asymmetric	Symmetric
CH_3	2962 ± 10	2872 ± 10
CH_2	2926 ± 10	2855 ± 10
CH_3-O	2970 - 2920	2830 ± 10

CH_2-O	2955 - 2920	2878 - 2835

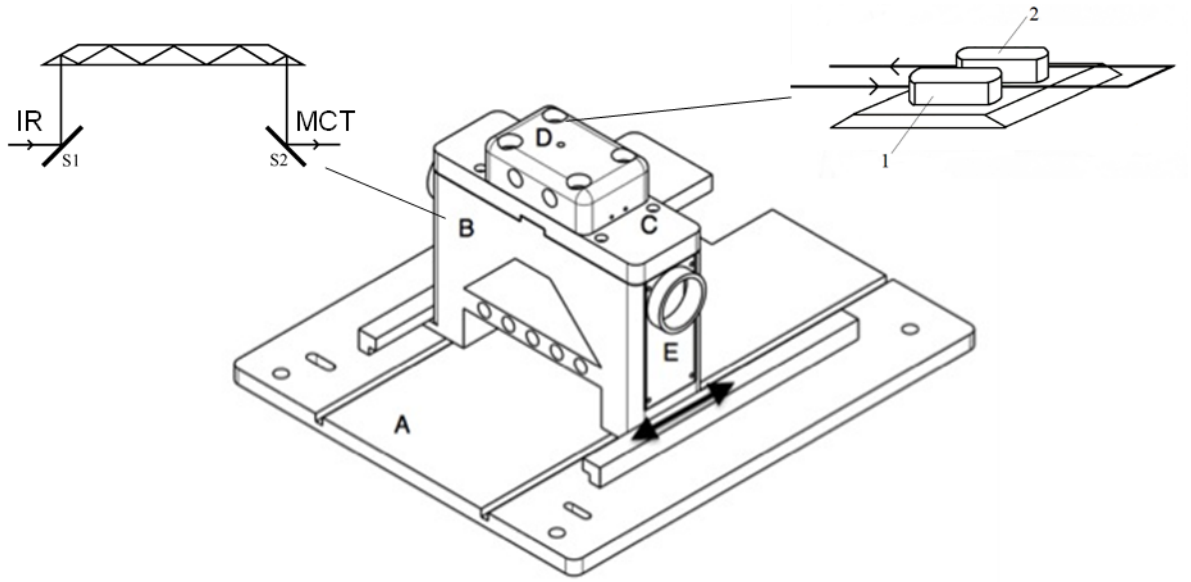

Figure S1. Schematic technical drawing of the home-made *in-situ* ATR-IR cell composed of the base unit (**A**) equipped with runners, reflector (**B**) with gold coated mirrors, ZnSe holder (**C**) with notch for IR beam, two chambers cell (**D**) with heating cartridges and thermocouple, connection to the N_2 purging lines (**E**).

The ATR-IR apparatus (see **Figure S1** for the technical drawing and **Figure S2** for a photograph) consists of five main parts. The base unit (A) enables a three-dimensional adjustment to align the cell within the spectrometer to the IR beam. Together with its runners, the ATR cell can be shifted forward and backward. The reflection unit (B) is connected to the base unit through complementary fittings to the runner lines. Within the reflection unit, two gold-coated mirrors reflect the IR beam to the top of the cell and back from the top to the detector. In the upper left corner of Figure 3 is an illustration of the IR beam path from the IR source to the reflecting mirror S1 to the ZnSe crystal with the crystal geometry of 27 x 20 x 2 mm^3 and a phase of 30° resulting in a total of nine reflections inside the crystal and to the S2 mirror. The crystal holder (C) is attached to the reflection unit, where four 3-mm notches are left for the IR beam to penetrate the ZnSe crystal. Within the ZnSe crystal, the IR beam undergoes in total nine reflections where three are in contact with the measured sample. On top of the ZnSe crystal, the double-chamber ATR cell (D) is attached and tightened up to the crystal holder with graphene gaskets. It is equipped with the feeding lines for both cell compartments, which are connected through 1/16-inch lines and inlets for heating cartridges and a thermocouple. In the upper right corner of **Figure S1** is a drawing of the cell design showing the two chambers and the flow of the liquid/gas feed, which goes first to chamber 1 and then passes through chamber 2. The volume of each chamber is around 0.3 ml, and the connecting line between chamber 1 and 2 has a volume of 0.02 ml.

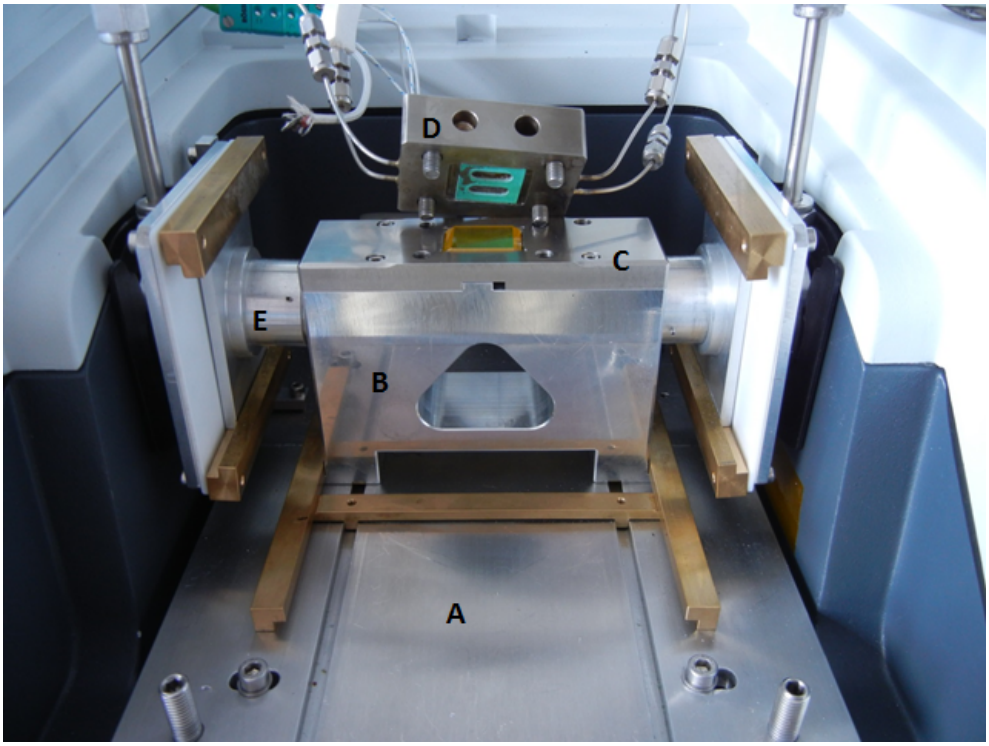

Figure S2. Photographed lab-built in-situ ATR-IR cell composed of the base unit (**A**) equipped with runners, reflector (**B**) with gold coated mirrors, ZnSe holder (**C**) with notch for IR beam, two chambers ATR cell (**D**) with temperature sensor and cartridge heaters, N_2 purging lines (**E**) adjustable to the forth and back movement of the cell.

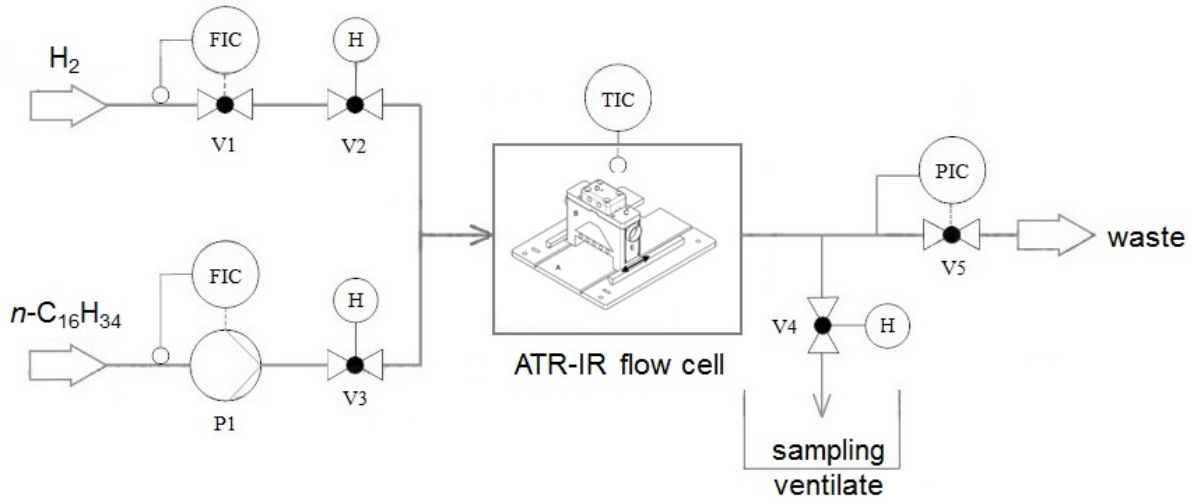

Figure S3. Schematic outline of the experimental set-up illustrating the peripheral arrangement of the ATR-IR apparatus.

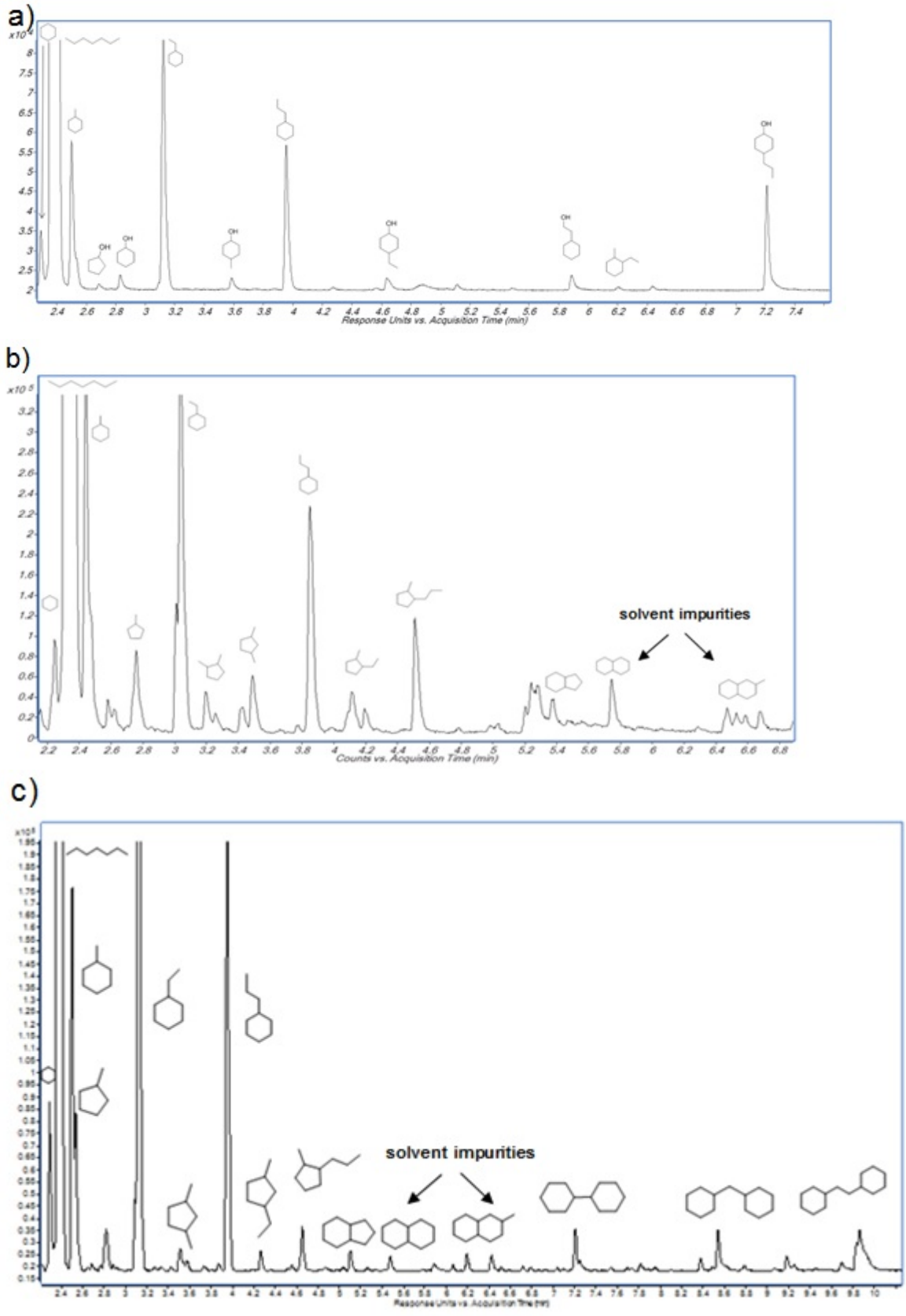

Figure S4. The representative gas chromatogram of reacted mixture liquid phase products after reaction of organosolv lignin (1 g) with a) 20 wt. % Ni/SiO_2 b) Ni/HZSM-5 and c) Ni/HBEA catalyst (each 0.5 g) and 100 ml hexadecane at 523 K, 20 bar H_2, 680 RPM, 6 h.

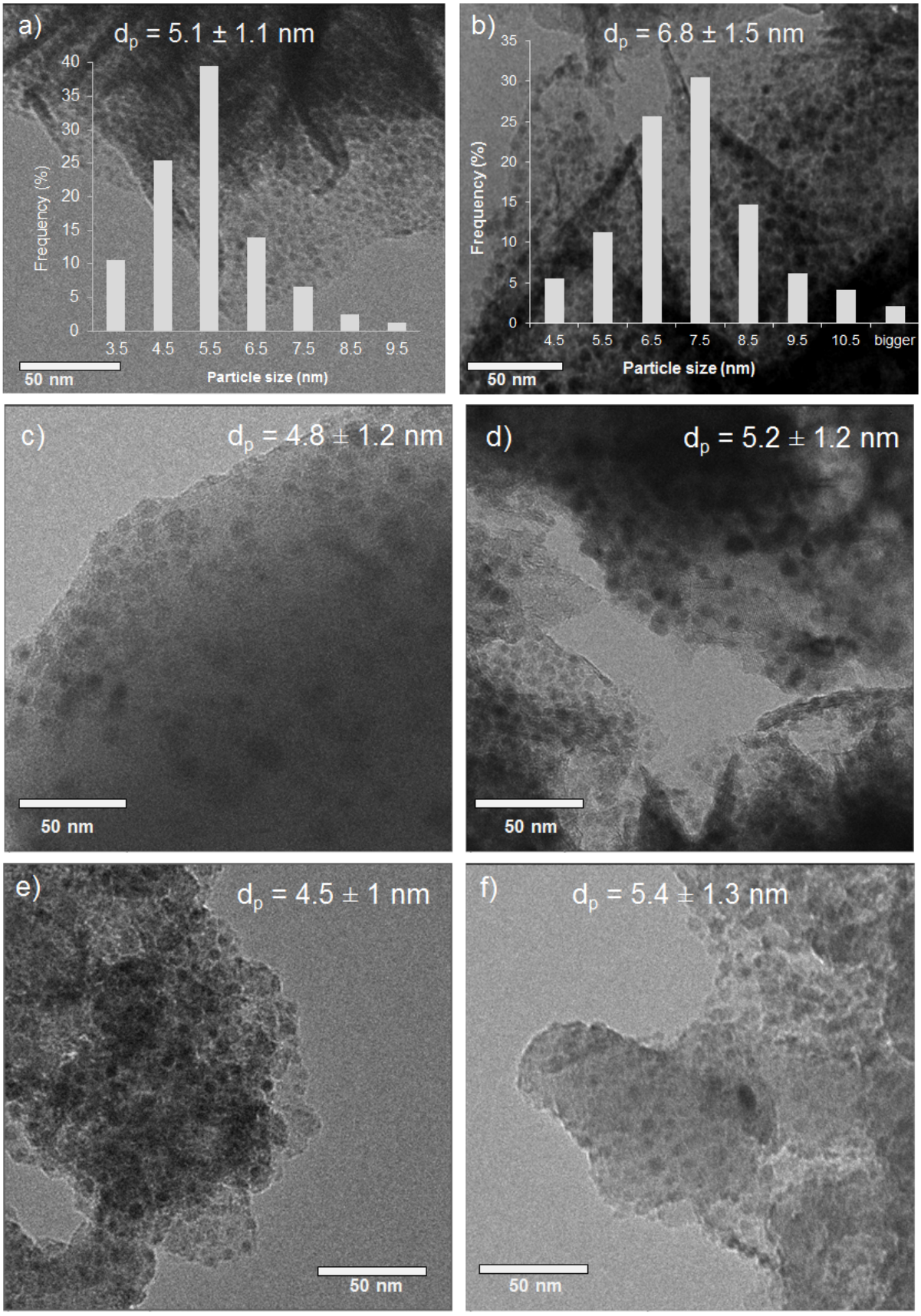

Figure S5. TEM of a) fresh Ni/HBEA catalyst, b) used Ni/HBEA**,** c) fresh Ni/HZSM-5 catalyst, d) used Ni/HZSM-5, e) fresh Ni/SiO_2 catalyst and f) used Ni/SiO_2**.**

As shown in **Figure S5**, after the catalyst was exposed to a reaction with Organosolv Lignin, the Ni particles increased in size by ca. 0.4 nm for HZSM-5, 0.9 nm for SiO_2 and 1.5 nm for HBEA supported Ni catalyst. The studied recycling runs (not shown here) showed a slight decrease in activity, which is mainly due to Ni particle growth *via* agglomeration and/or Ostwald ripening as already described in previous studies for aqueous phase hydrodeoxygenation of phenol [10] and non-polar liquid phase hydrodeoxygenation of stearic acid. [11]

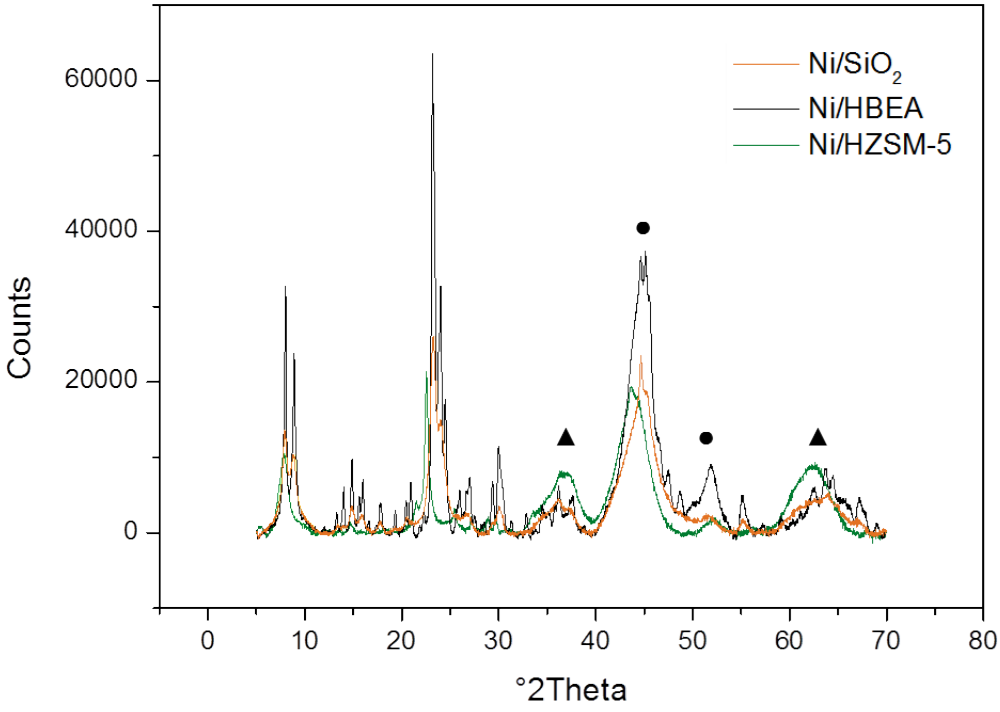

Figure S6. X-ray diffraction pattern of Ni catalysts, i.e., Ni/SiO_2, Ni/HZSM-5, Ni/HBEA, where ▲ corresponds to NiO phase and ● to metallic Ni.

The X-ray diffraction patterns of three Ni catalysts are shown in **Figure S6**. The crystalline sizes for both metallic crystalline phases Ni(111) and Ni(200) were calculated using the Scherrer equation. For Ni/SiO_2 the crystalline size of Ni(111) phase at 2θ of 45° was calculated to be 2.5 nm, the Ni(200) at 2θ of 51° size was found to be 4.1 nm. For Ni/HBEA the Ni(111) size was calculated to the value of 3.5 nm, whereas the Ni(200) was 5.8 nm. For Ni/HZSM-5 catalyst the Ni(111) was 2.9 nm and the Ni(200) was calculated to the value of 4.5 nm. The Scherrer equation derived Ni crystalline sizes are in good agreement with the measured Ni cluster sizes in TEM pictures (**Figure S5)**.

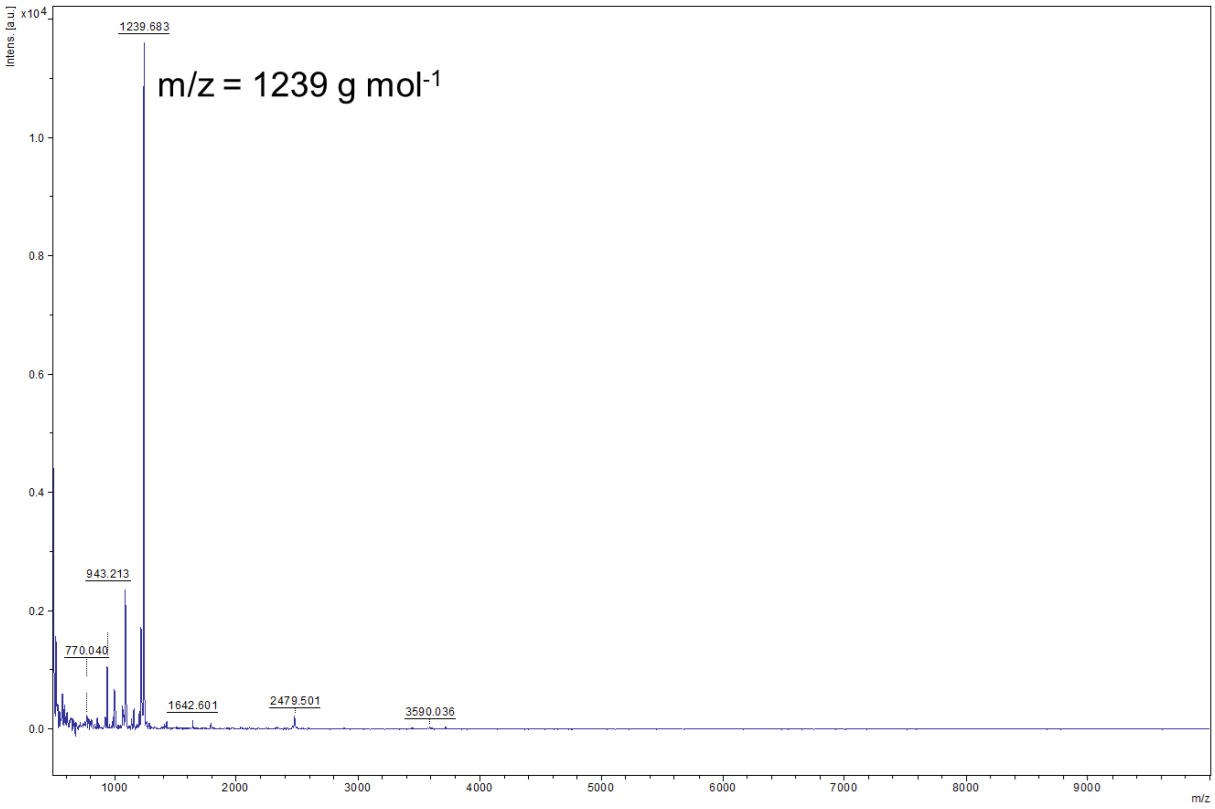

Figure S7. Matrix-assisted Laser Desorption/Ionization Time-Of-Flight Mass Spectrometry (MALDI-TOF MS) of organosolv lignin.

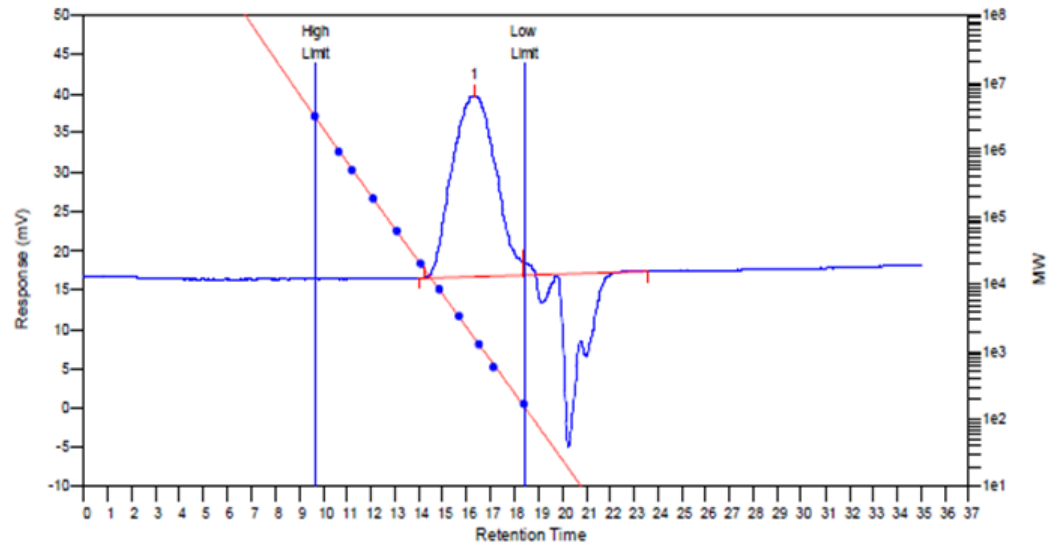

MW Averages

Peak No	Mp	Mn	Mw	Mz	Mz+1	Mv	PD
1	1654	1107	2261	3982	5769	2049	2.04246

Figure S8. Gel permeation chromatography (GPC) analysis of organosolv lignin in anhydrous tetrahydrofuran (THF) with a concentration of 1 mg ml^{-1}.

A thermogravimetric analysis of the organosolv lignin and the solid residue after Ni catalyzed reaction reveals a substantial difference in thermal decomposition behavior (**Figure S9**).

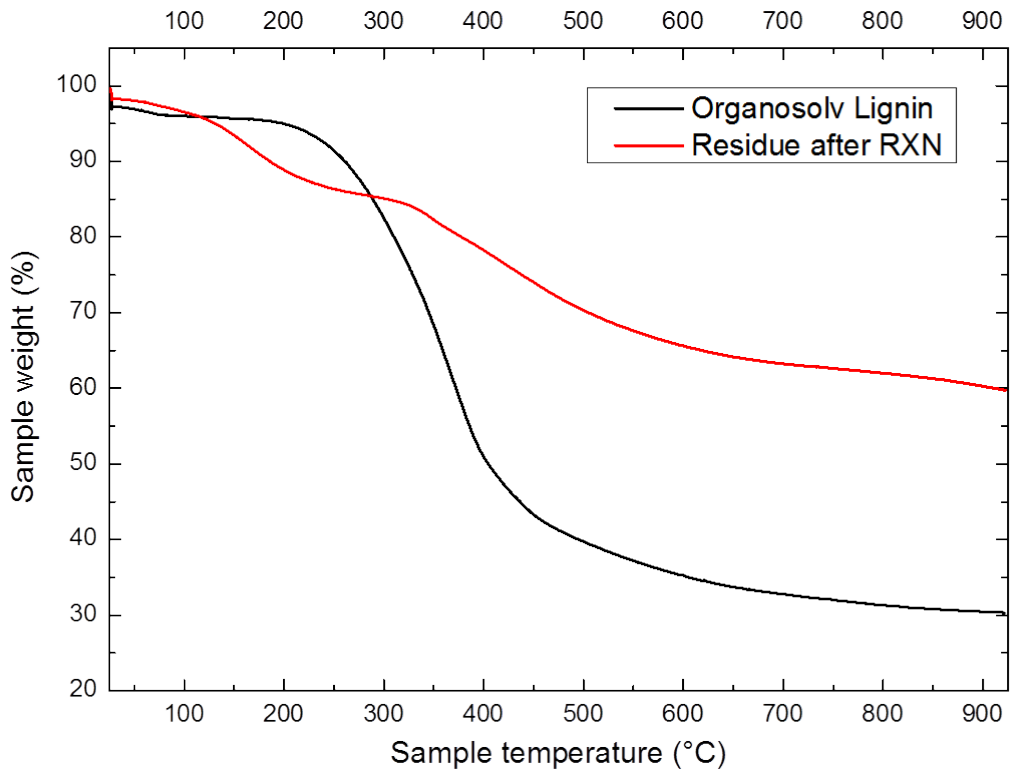

Figure S9. Thermogravimetric analysis (TGA) of the organosolv lignin and the solid residue (separated from catalyst) after reaction with Ni/HBEA catalyst at 523 K and 2 MPa H_2 and 4 h reaction time at 700 RPM.

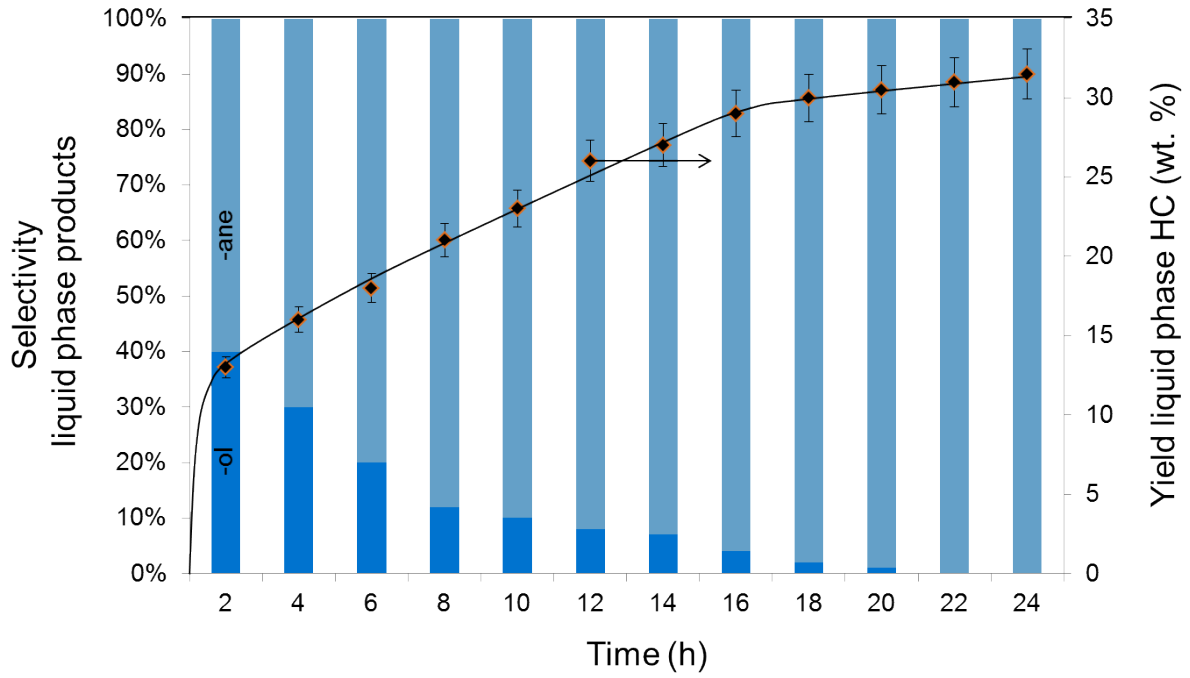

Figure S10. Hydro-deconstruction of organosolv lignin on Ni/SiO_2 catalysts as a function of contact time at the following conditions: organosolv lignin (1 g), 20 wt.% Ni/SiO_2 (0.5 g), 523 K, 2 MPa H_2 charged before reaction started, 700 RPM.

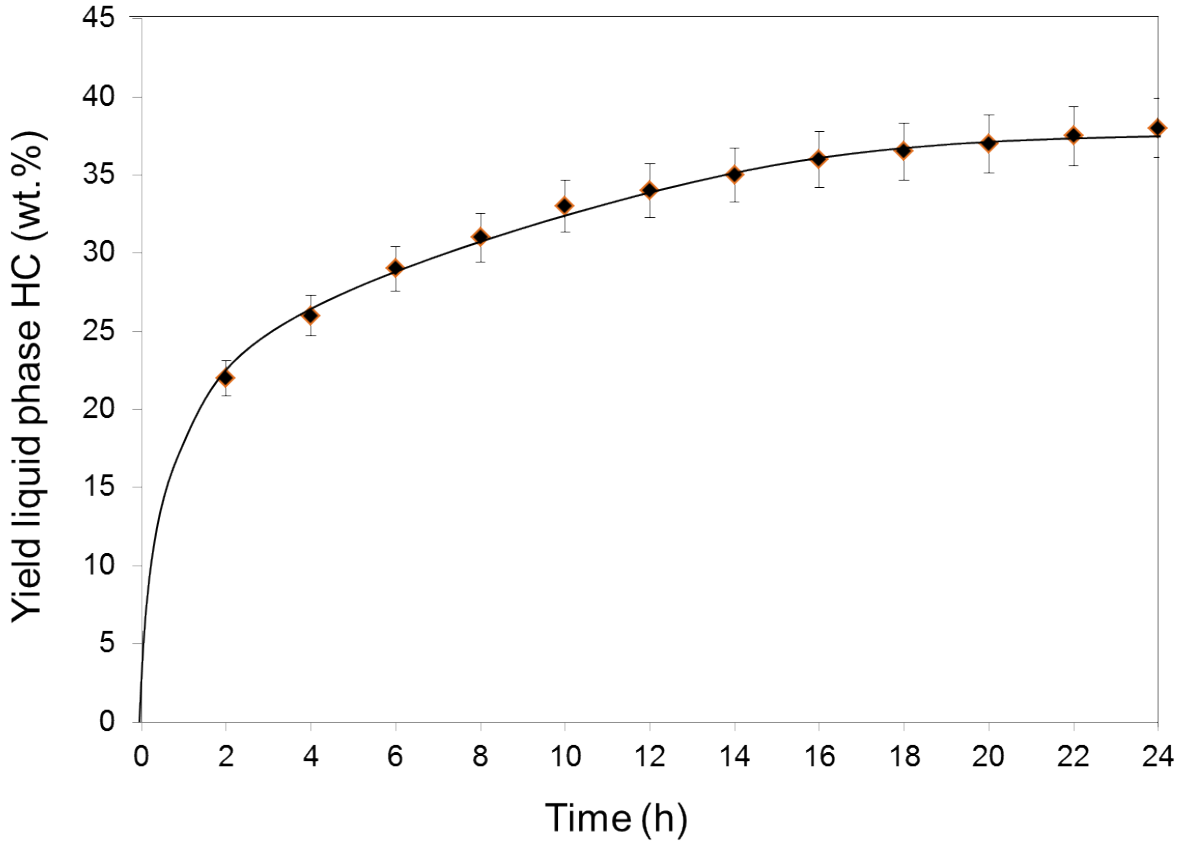

Figure S11. Conversion of organosolv lignin on Ni/HZSM-5 as a function of contact time at the following conditions: organosolv lignin (1 g), 21 wt. % Ni/HZSM-5 (0.5 g), 523 K, 2 MPa H_2 charged before reaction started, 700 RPM.

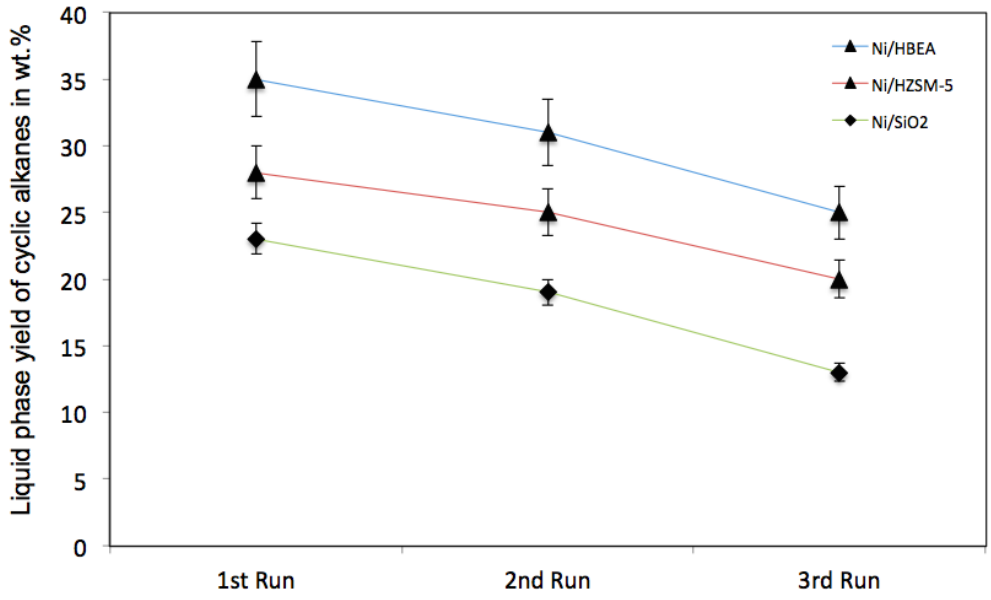

Figure S12. Recycling runs with Ni/HBEA (blue line), Ni/HZSM-5 (red line) and Ni/SiO_2 (green line) catalysts at reaction conditions: 523 K, 2 MPa H_2 at ambient conditions, 100 ml *n*-$C_{16}H_{34}$, 680 RPM, 6 h.

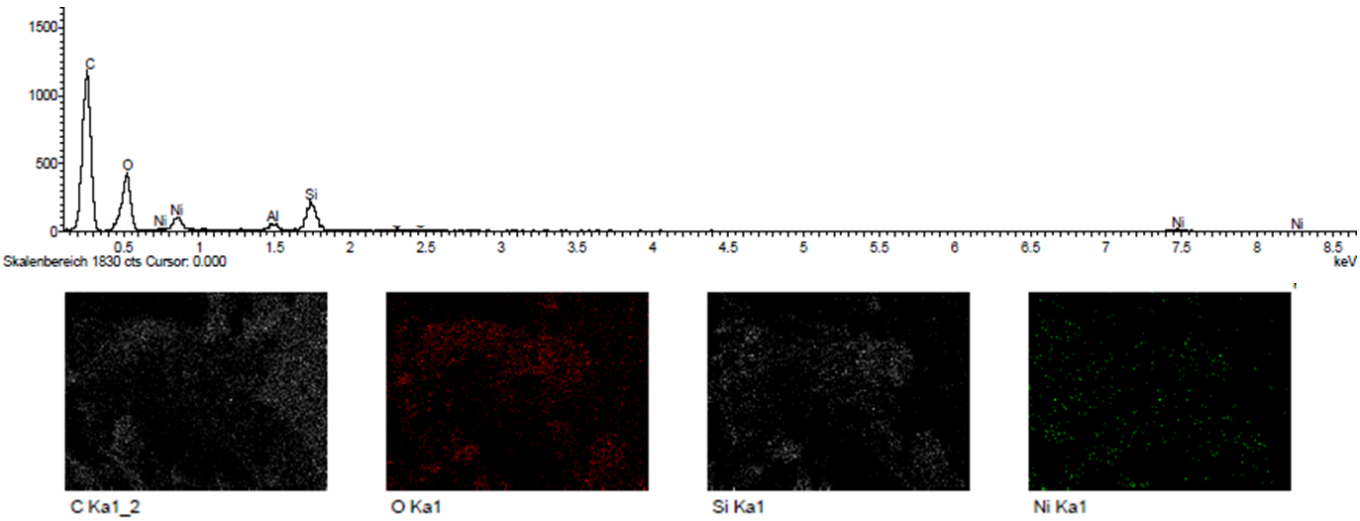

Figure S13. EDX spectra during the HR-SEM measurements mapping the elemental distribution (C, O, Si and Ni) across the coated film containing lignin and Ni/HBEA catalyst.

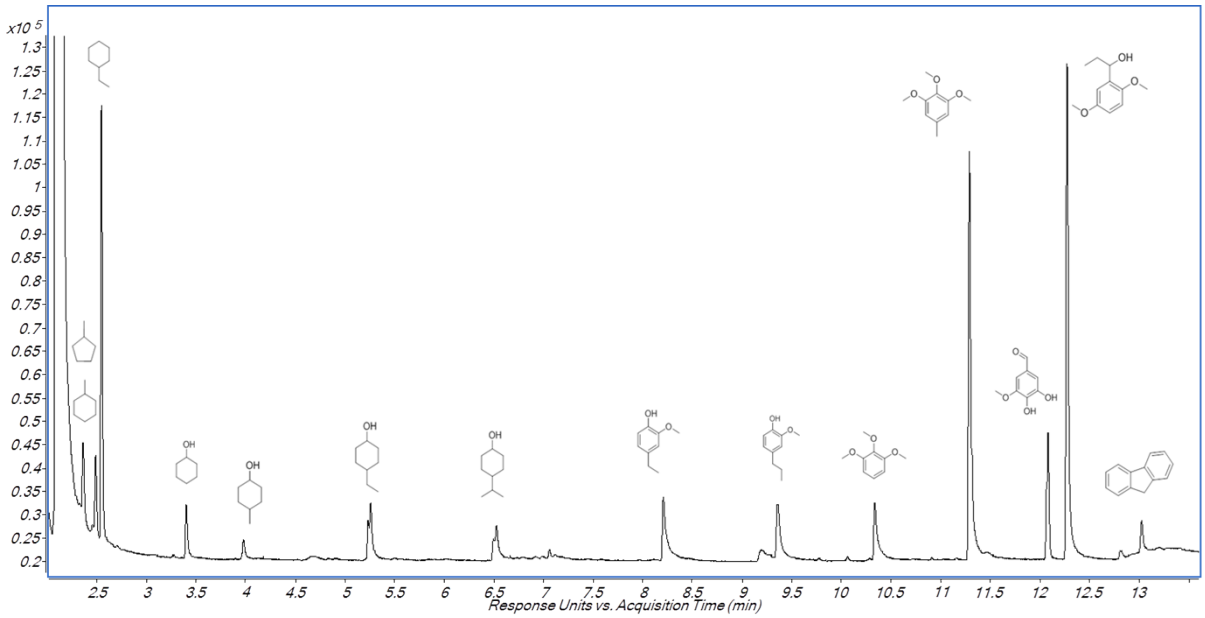

Figure S14. Gas chromatogram of liquid phase aliquot taken during *in situ* ATR-IR studies at a contact time of 90 minutes. Catalyst: Ni/HBEA.

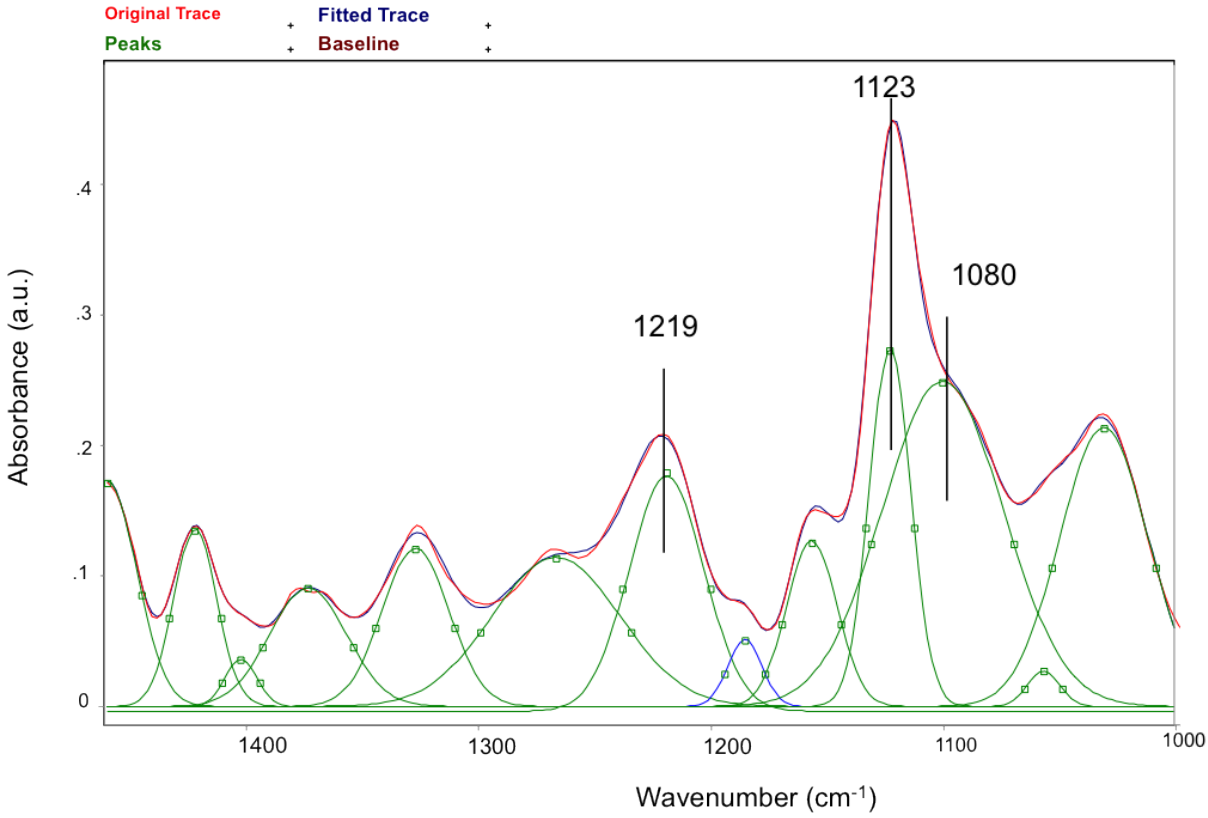

Figure S15. An example of the band deconvolution for the third spectral region (shown in Figure 4 of the main text) in the in-situ ATR-IR spectra at t = 0 min (i.e., at the start of the liquid n-hexadecane flow), where the peaks centered at 1219, 1123 and 1080 cm^{-1} are assigned to the asymmetric C-C-O stretching vibrations.

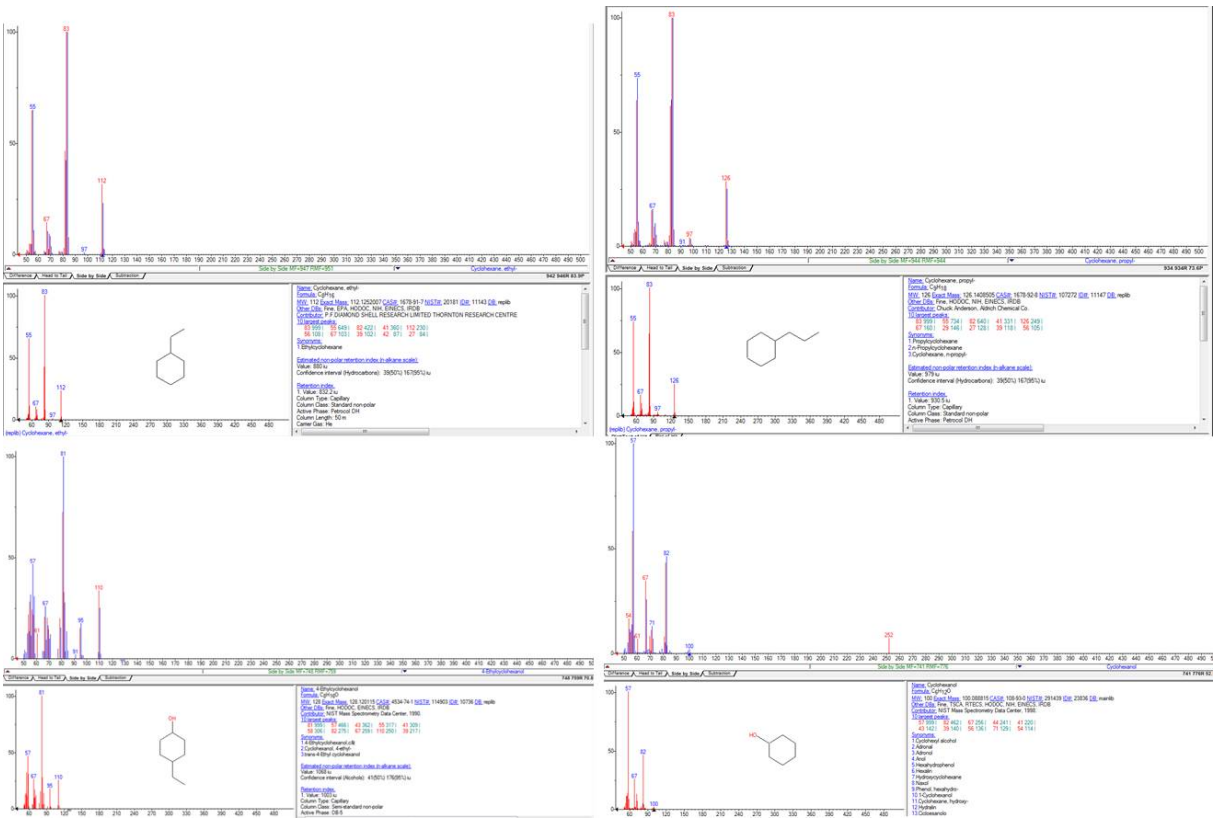

Figure S16. MS ions pattern of the representative molecules in the reaction mixtures.

References:

1. P. Burattin, M. Che and C. Louis, *The Journal of Physical Chemistry B*, 1998, **102**, 2722-2732.
2. R. Nares, J. Ramírez, A. Gutiérrez-Alejandre, C. Louis and T. Klimova, *The Journal of Physical Chemistry B*, 2002, **106**, 13287-13293.
3. W. Song, Y. Liu, E. Baráth, C. Zhao and J. A. Lercher, *Green Chemistry*, 2015, **17**, 1204-1218.
4. C. Zhao and J. A. Lercher, *ChemCatChem*, 2012, **4**, 64-68.
5. C. Zhao, Y. Kou, A. A. Lemonidou, X. Li and J. A. Lercher, *Angewandte Chemie International Edition*, 2009, **48**, 3987-3990.
6. C. Zhao, Y. Kou, A. A. Lemonidou, X. Li and J. A. Lercher, *Chemical Communications*, 2010, **46**, 412-414.
7. C. Zhao, J. He, A. A. Lemonidou, X. Li and J. A. Lercher, *Journal of Catalysis*, 2011, **280**, 8-16.
8. J. He, C. Zhao and J. A. Lercher, *Journal of the American Chemical Society*, 2012, **134**, 20768-20775.
9. B. C. Smith, *Infrared spectral interpretation: a systematic approach*, CRC press, 1998.
10. C. Zhao, S. Kasakov, J. He and J. A. Lercher, *Journal of Catalysis*, 2012, **296**, 12-23.
11. W. Song, C. Zhao and J. A. Lercher, *Chemistry – A European Journal*, 2013, **19**, 9833-9842.